

# 1 Comparing synthetic refocusing to deconvolution for the extraction 2 of neuronal calcium transients from light-fields

3 **Carmel L. Howe<sup>a,b</sup>, Peter Quicke<sup>a,b</sup>, Pingfan Song<sup>b</sup>, Herman Verinaz Jadan<sup>b</sup>, Pier Luigi  
4 Dragotti<sup>b</sup>, Amanda J. Foust<sup>a,b,\*</sup>**

5 <sup>a</sup>Department of Bioengineering, Imperial College London, London, UK

6 <sup>b</sup>Centre for Neurotechnology, Imperial College London, London, UK

7 <sup>c</sup>Department of Electrical and Electronic Engineering, Imperial College London, London, UK

## 8 **Abstract.**

9 **Significance:** Light-field microscopy (LFM) enables fast, light-efficient, volumetric imaging of neuronal activity with  
10 calcium indicators. Calcium transients differ in temporal signal-to-noise ratio (tSNR) and spatial confinement when  
11 extracted from volumes reconstructed by different algorithms.

12 **Aim:** We evaluated the capabilities and limitations of two light-field reconstruction algorithms for calcium fluores-  
13 cence imaging.

14 **Approach:** We acquired light-field image series from neurons either bulk-labeled or filled intracellularly with the red-  
15 emitting calcium dye CaSiR-1 in acute mouse brain slices. We compared the tSNR and spatial confinement of calcium  
16 signals extracted from volumes reconstructed with synthetic refocusing and Richardson-Lucy 3D deconvolution with  
17 and without total variation regularization.

18 **Results:** Both synthetic refocusing and Richardson-Lucy deconvolution resolved calcium signals from single cells  
19 and neuronal dendrites in three dimensions. Increasing deconvolution iteration number improved spatial confinement  
20 but reduced tSNR compared to synthetic refocusing. Volumetric light-field imaging did not decrease calcium signal  
21 tSNR compared to interleaved, widefield image series acquired in matched planes.

22 **Conclusions:** LFM enables high-volume rate, volumetric imaging of calcium transients in single cells (bulk-labeled),  
23 somata and dendrites (intracellular loaded). The trade-offs identified for tSNR, spatial confinement, and computa-  
24 tional cost indicate which of synthetic refocusing or deconvolution can better realize the scientific requirements of  
25 future LFM calcium imaging applications.

26 **Keywords:** light-field microscopy, calcium imaging, fluorescence imaging, deconvolution.

27 \*Amanda J. Foust, [a.foust@imperial.ac.uk](mailto:a.foust@imperial.ac.uk)

## 28 **1 Introduction**

29 Understanding how neuronal networks learn, process, and store information requires imaging tech-  
30 niques capable of monitoring the activity of hundreds to thousands of neurons simultaneously in  
31 three-dimensional (3D) tissues. Capturing rapid neuronal calcium dynamics requires high tem-  
32 poral resolution at cellular or subcellular spatial resolution.<sup>1</sup> The development of synthetic and  
33 genetically-encoded fluorescent indicators of intracellular calcium concentration<sup>2,3</sup> and membrane  
34 voltage<sup>4,5</sup> enables functional imaging on these scales.

35 The optical sectioning capability of confocal and multi-photon scanning microscopes adapts  
36 them well to 3D imaging of scattering brain tissues. However, scanning limits the fluorescence  
37 bandwidth and hence the acquisition speed and temporal signal-to-noise ratio (tSNR). tSNR de-  
38 scribes the ability to discriminate transient changes in fluorescence from baseline noise. For shot  
39 noise-limited systems, tSNR is proportional to the square-root of the collected fluorescence photon  
40 flux. That is why applications requiring high acquisition rates and/or SNR typically rely on wide-  
41 field, single-photon imaging to maximize photon flux by exciting fluorescence simultaneously in  
42 all illuminated structures. Widefield excites fluorescence efficiently throughout a volume, how-  
43 ever, only one axial plane is imaged. In this configuration, fluorescence excited above and below  
44 the imaging plane is not only unnecessary, but contributes spurious fluorescence to the in-focus  
45 image, degrading contrast and confusing the functional signals.<sup>6</sup>

46 Light-field microscopy (LFM) exploits out-of-focus fluorescence simultaneously excited through-  
47 out the volume. LFM combined with widefield, single-photon fluorescence excitation enables vol-  
48 umetric collection, maximizing the photon budget. LFM is a 3D imaging technique, which encodes  
49 both lateral position and angular information, unlike conventional imaging that focuses on objects  
50 in a single plane.<sup>7</sup> A microlens array (MLA) at the microscope's native image plane enables image  
51 reconstruction at different planes and perspectives from a single light-field image. This increases  
52 light efficiency and speed at the cost of spatial resolution as the cameras pixels now divide over  
53 four-dimensions  $(x, y, \theta_x, \theta_y)$  rather than two  $(x, y)$ . The four-dimensional light-field can be used to  
54 reconstruct a volume around the native focal plane, slice by slice. Two methods for reconstruct-  
55 ing volumes from LFM images are commonly used: synthetic refocusing<sup>7</sup> and 3D deconvolution.<sup>8</sup>  
56 Synthetic refocusing extracts single planes from a light-field that correspond to widefield images.  
57 Multiple planes can be reconstructed orthogonal to the optical axis to generate a  $z$ -stack. Synthetic

58 refocusing is computationally fast as each pixel in the output volume is simply the weighted sum  
59 of a subset of pixels in the light-field. However, similar to widefield imaging, this technique lacks  
60 optical sectioning such that out-of-focus sources reduce the contrast of in-focus sources. In con-  
61 trast, 3D deconvolution reconstructs a volume by deconvolving its light-field measurements with  
62 a 3D light-field Point Spread Function (PSF) based on a wave optics model<sup>9</sup> of the LFM. This can  
63 be achieved by using iterative deconvolution methods, such as the Richardson-Lucy<sup>10,11</sup> or Im-  
64 age Space Reconstruction Algorithms.<sup>12</sup> 3D deconvolution can achieve a higher spatial resolution  
65 than synthetic refocusing because the individual projections through the volume sample the object  
66 more finely than the microlens array, thus improving the discriminability of signals in 3-dimensions.  
67 However, 3D deconvolution approaches are computationally intensive and amplify noise.<sup>13</sup>

68 LFM's capacity to capture volumetric data from 2D frames has recently motivated its applica-  
69 tion to imaging neuronal activity in non-scattering specimens such as *C. Elegans* and Zebrafish,<sup>14-19</sup>  
70 and in mammalian brain *in vivo*.<sup>20-22</sup> Seeded iterative demixing<sup>20,22</sup> and compressive LFM<sup>15</sup> in-  
71 crease the speed of neuronal localization and single-cell time series analysis by identifying and  
72 localizing somatic signals. Notably, these techniques improved performance in scattering brain  
73 tissues compared to volume reconstruction methods that only account for ballistic photons. How-  
74 ever, volume reconstruction is still necessary to image the generation and propagation of voltage  
75 and calcium transients spatially extended structures such as axons and dendrites.

76 Here we show that LFM can resolve calcium transients simultaneously in axially separated  
77 somata and dendrites of neurons loaded with a red-emitting calcium dye, CaSiR-1.<sup>23</sup> We exam-  
78 ined trade-offs between the tSNR and the spatial signal confinement of calcium signals localized in  
79 volumes reconstruction from light fields by synthetic refocusing and 3D deconvolution. A compar-  
80 ison of calcium signals extracted from interleaved light-field and widefield imaging trials showed

81 no penalty to tSNR for light-field trials, which additionally enabled localization of calcium signals  
82 in 3D. These results demonstrate the power of LFM for simultaneously tracking calcium transients  
83 in axially separated neurons and neuronal subcompartments. By distilling the trade-offs between  
84 spatial signal confinement and tSNR, these results underline the importance of selecting a volume  
85 reconstruction method adapted to the scientific goals of future experiments.

## 86 **2 Materials and Methods**

87 Parts of the following methods and preliminary SNR quantification results were published in Howe  
88 *et al.* (2020).<sup>24</sup>

### 89 *2.1 Optical System*

90 We designed our LFM following Levoy *et al.* (2006).<sup>7</sup> Imaging was performed with a custom-built  
91 epifluorescence microscope with a MLA (125  $\mu\text{m}$  pitch, f/10, RPC Photonics) placed at the imag-  
92 ing plane of a 25 $\times$ , Numerical Aperture (NA)=1.0 water immersion objective lens (XLPLN25XSVMF,  
93 Olympus) and 180 mm tube lens (TTL180-A, Thorlabs), illustrated in Figure 1A. The MLA was  
94 imaged onto a scientific complementary metal-oxide-semiconductor (sCMOS) camera (ORCA  
95 Flash 4 V2 with Camera Link, 2048 $\times$ 2048 pixels, 6.5  $\mu\text{m}$  pixel size, Hamamatsu) with a 1:1 relay  
96 macro lens (Nikon 60 mm f2.8 D AF Micro Nikkor Lens).

97 The LFM image consists of circular subimages (Figure 1B) which are parameterized by the 4D  
98 function  $\mathcal{L}(u, v, x, y)$ , where each lenslet is  $\mathcal{L}(u, v, \cdot, \cdot)$  and the same pixel in each lenslet subimage  
99 is  $\mathcal{L}(\cdot, \cdot, x, y)$ . Each circular subimage represents the angular content of the light at a specific spatial  
100 location.

101 The ‘native LFM spatial resolution’ is given by the microlens pitch divided by the objective



102 magnification. Therefore, an MLA was chosen such that the lateral resolution of our LFM was  
103  $5\ \mu\text{m}$ , roughly half the diameter of a cortical neuron ( $10\ \mu\text{m}$ ). The axial resolution of a LFM is  
104 defined by the number of resolvable diffraction-limited spots behind each microlens.<sup>7</sup> Using the  
105 Sparrow criterion and assuming a peak emission wavelength of  $664\ \text{nm}$  ( $\lambda$ ) for CaSiR-1,<sup>23</sup> the spot  
106 size in the camera plane is  $7.64\ \mu\text{m}$ . So, with a  $125\ \mu\text{m}$  pitch MLA, we are able to resolve  $N_u = 13$   
107 distinct spots under each microlens. The depth of field when synthetically refocusing is given by  
108 eq. (1), resulting in a depth of field of  $6.52\ \mu\text{m}$ <sup>7</sup> compared to  $0.8\ \mu\text{m}$  in a conventional widefield  
109 microscope with the same imaging parameters.

$$D = \frac{(2 + N_u)\lambda n}{2NA^2} \quad (1)$$

110 where  $n$  is the refractive index.

## 111 2.2 Brain slice preparation

112 This study was carried out in accordance with the recommendations of the UK Animals (Scientific  
113 Procedures) Act 1986 under Home Office Project and Personal Licenses (project license 70/9095).  
114  $400\ \mu\text{m}$  slices were prepared from 33 to 196 day old mice using the ‘protective recovery’ method.<sup>25</sup>  
115 Slices were cut in Na-aCSF containing (in mM): 125 NaCl, 25 NaHCO<sub>3</sub>, 20 glucose, 2.5 KCl, 1.25  
116 NaH<sub>2</sub>PO<sub>4</sub>, 2 MgCl<sub>2</sub>, 2 CaCl<sub>2</sub>. After cutting, the slices were transferred for a period of 12 minutes to  
117 a solution containing (in mM) 110 N-Methyl-D glucamine, 2.5 KCl, 1.2 NaH<sub>2</sub>PO<sub>4</sub>, 25 NaHCO<sub>3</sub>,  
118 25 Glucose, 10 MgCl<sub>2</sub>, 0.5 CaCl<sub>2</sub>, adjusted to 300 – 310 mOsm/kg, pH 7.3 – 7.4 with HCl at  
119  $36^\circ\text{C}$ , before being transferred back to the first solution for at least an hour before imaging trials.  
120 All solutions were oxygenated with 95% O<sub>2</sub>/5% CO<sub>2</sub>.

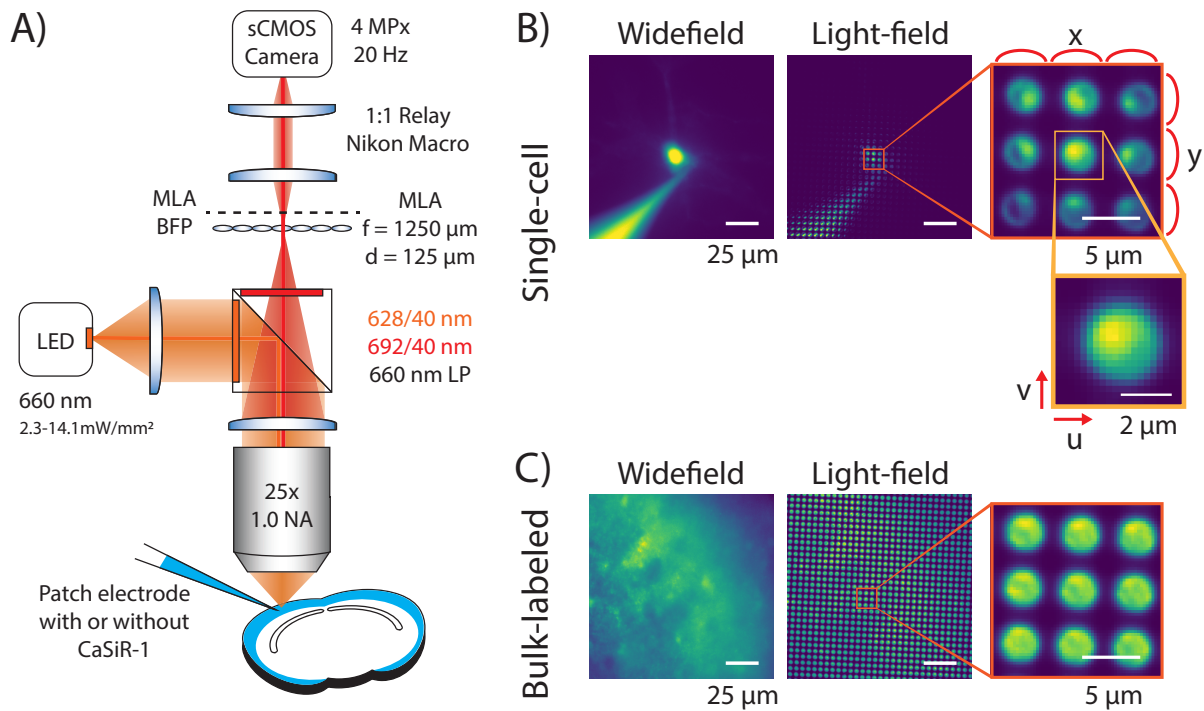


**Fig 1** A) Optical system schematic. A microlens array is placed at the native imaging plane of a widefield microscope and the back focal plane is imaged onto a sCMOS camera enabling 3D reconstructions from a 2D frame. B) Example widefield and light-field images from both a single neuron intracellularly loaded with the synthetic calcium dye, CaSiR-1 via a micropipette. Close-up views of the raw light-field images show the circular subimages encoding the 4D spatial and angular information. The light-field is parameterized by a 4D function,  $\mathcal{L}(u, v, x, y)$ , where each lenslet is  $\mathcal{L}(u, v, \cdot, \cdot)$  and the same pixel in each lenslet subimage is  $\mathcal{L}(\cdot, \cdot, x, y)$ . C) Example images from bulk-labeled slices where CaSiR-1 AM was bath applied to many neurons.

121 After resting the slices were either bulk-labeled with CaSiR-1 AM-ester dye or used for single-  
 122 cell labeling with CaSiR-1 potassium salt.

123 For bulk-labeled slices 50  $\mu\text{g}$ , CaSiR-1 AM (GC402, Goryo Chemicals)<sup>23</sup> was dissolved in 10  $\mu\text{l}$   
 124 of dimethyl sulfoxide (DMSO) with 10% w/v Pluronic F-127 (Invitrogen) and 0.5% v/v Kolliphor  
 125 EL (Sigma-Aldrich).<sup>26</sup> The slices were then incubated for 40 minutes at 37°C in 2 ml of Na-  
 126 aCSF with the CaSiR-1 AM/DMSO mixture pipetted onto the surface of each slice, oxygenated  
 127 by blowing 95% O<sub>2</sub>/5% CO<sub>2</sub> onto the surface. After loading, the slices rested in room temperature  
 128 Na-aCSF for at least 20 minutes before use.

### 129 2.3 Imaging

130 For single-cell labeling, cortical cells were patched using 6 – 8 MOhm patch pipettes containing  
131 intracellular solution consisting of (in mM): 130 K-Gluconate, 7 KCl, 4 ATP-Mg, 0.3 GTP-Na, 10  
132 Phosphocreatine-Na, 10 HEPES, 0.1 CaSiR-1 potassium salt (GC401, Goryo Chemicals).<sup>23</sup> After  
133 sealing and breaking in, the calcium dye was allowed to diffuse into the cell (Figure 1B). For bulk-  
134 labeled slices (Figure 1C), cortical cells were patched containing the same intracellular solution  
135 without the addition of the CaSiR-1 potassium salt.

136 Cells were patched under oblique light-emitting diode (LED) infrared illumination (peak 850  
137 nm). The signals were recorded with a Multiclamp 700B amplifier (Axon Instruments) and digi-  
138 tized with a Power 1401 (Cambridge Electronic Design).

139 Imaging trials were taken at 20 frames/s at room temperature. Stimulation consisted of five  
140 current pulses for 10 ms at 0.5 Hz where the current was adjusted to stimulate a single action  
141 potential. For single cells, this stimulus was applied to the labeled cell with the dye-loading pipette.  
142 For bulk-labeled slices, the stimulus was applied to a cell in the field of view causing broader  
143 activation of multiple neurons in the local network. Widefield and light-field trials were interleaved  
144 by removing and replacing the MLA from a precision magnetic mount (CP44F, Thorlabs). The  
145 removal and addition of the MLA shifted the focal sample plane. We calculated this focal plane  
146 shift using the thin lens equation to be  $\pm 2 \mu\text{m}$ .

147 Fluorescence was excited with a 660 nm LED (M660L2, Thorlabs) powered by a constant  
148 current source (Keithley Sourcemeter 1401) to illuminate the sample between 2.3-14.1 mW/mm<sup>2</sup>.  
149 The 660 nm LED was collimated with an  $f = 16$  mm aspheric lens (ACL25416U0-A, Thorlabs)  
150 and filtered with a 628/40 nm excitation filter (FF02-628/40, Semrock). Collected fluorescence

151 was filtered with a 660 nm long-pass dichroic (FF660-Di02, Semrock) along with a 692/40 nm  
152 emission filter (FF01-692/40, Semrock). Imaging data were acquired with Micromanager.<sup>27</sup>

153 Single-cell labeled somata laid between 46 and 49  $\mu\text{m}$  below the slice surface, with a median  
154 depth of 47 [IQR, 46.2, 48.6]  $\mu\text{m}$ . Whereas bulk-labeled somata were between 29 and 36  $\mu\text{m}$  below  
155 the slice surface, with a median depth of 34 [30, 34.8]  $\mu\text{m}$ .

#### 156 2.4 Light-field volume reconstruction

157 We reconstructed light-field source volumes from the raw light-fields (Figure 1B&C) using syn-  
158 thetic refocusing<sup>7</sup> and Richardson-Lucy (RL) 3D deconvolution.<sup>8,10,11</sup> Images synthetically refo-  
159 cused at a plane  $f' = \alpha f_0$ , where  $f_0$  is the native focal plane, were calculated from a light-field  
160 image parameterized by  $\mathcal{L}(x, y, u, v)$  using the formula derived in<sup>28</sup> as

$$I(x, y) = \sum_{u,v} \mathcal{L}(x + u(1 - 1/\alpha), y + v(1 - 1/\alpha), u, v), \quad (2)$$

161 where  $I(x, y)$  represents the refocused image. This process can be interpreted as a summation over  
162 different shifted angular ‘views’ of the sample represented by  $\mathcal{L}(x, y, \cdot, \cdot)$  such that the rays forming  
163 the views intersect at the desired refocus plane. We synthetically refocused ‘stacks’ of images or  
164 image time series,  $I(x, y, z, t)$  at 1  $\mu\text{m}$   $z$ -intervals using linear interpolation of the collected light-  
165 field images or videos.

166 Stacks from the same light-field images were also calculated using RL deconvolution. The 3D  
167 light-field PSF was calculated using the method described in,<sup>9</sup> by considering how a LFM collects  
168 fluorescence from a dipole oscillating with a wavelength of 550 nm. The total PSF was calculated  
169 as an incoherent sum of dipoles oriented along  $x$ ,  $y$ , and  $z$ . PSF values were calculated on a  $5 \times 5$

170 grid relative to the microlens. A low resolution PSF was calculated by averaging over the PSF  
171 values weighted by a 2D Hamming window of a width equal to the MLA pitch and coaxial with  
172 the lens. The estimated volume,  $x$ , is recovered from the measured light-field image,  $y$ , and the  
173 PSF,  $H$  using the following iterative update scheme in matrix-vector notation:

$$x^{k+1} = \frac{1}{a} \left[ H^T \frac{y}{Hx^k} \right] x^k, \quad (3)$$

174 where the fraction  $y/Hx^k$  is computed element-wise and  $a = \sum_i H(i, :)$ . Stacks were recon-  
175 structed using this method as with synthetic refocusing for varying numbers of iterations of eq.  
176 3.

177 Additionally, to enhance edges and reduce noise, we slightly modified the objective function  
178 of RL to include a total variation (TV) term, as in.<sup>29</sup> To incorporate this regularization prior, we  
179 modified the standard RL as follows

$$x^{k+1} = H^T \left( \frac{y}{Hx} \cdot \frac{x^k}{a - \lambda \operatorname{div} \left( \frac{\nabla x^k}{|\nabla x^k|} \right)} \right), \quad (4)$$

180 where  $\operatorname{div}$  is the divergence operator,  $\nabla$  is the gradient operator, and  $\lambda$  is a regularization factor set  
181 to 0.01, determined by visual inspection of the volumes.

## 182 2.5 Time Series Analysis

### 183 2.5.1 SNR

184 Signals were extracted from widefield or light-field time series reconstructed with synthetic refo-  
185 cusing or RL 3D deconvolution.

We calculated  $\Delta F/F$  using eq. (5) where  $F$  was the raw fluorescent signal,  $F_0$  was the baseline fluorescence taken as an average prior to the action potential, and  $F_d$  was the camera's dark signal (all in counts).

$$\frac{\Delta F}{F} = \frac{F - F_0}{F_0 - F_d} \quad (5)$$

186 An 'activation map' was produced from the variance over time to indicate the pixels containing  
187 the greatest temporal signal from the  $\Delta F/F$  map. Regions of interest (ROI) were defined by  
188 extracting the top 2 percentile of signal containing pixels (somatic and dendritic).

189 The SNR was calculated by dividing the peak signal (%) by the baseline noise (%), given by  
190 the square-root of the variance of the baseline fluorescence taken as an average prior to the action  
191 potential (20 samples, 1 second).

## 192 2.6 Statistics

193 All statistics are reported as median [inter-quartile range (IQR)]. Wilcoxon matched-pairs signed-  
194 rank test was performed between synthetically refocused and 3D deconvolved light-field time se-  
195 ries. These reconstructions were generated from the same image series, removing independent  
196 variables such as bleaching and changes in dye loading in the case of single-cell labeling. Statisti-  
197 cal analysis was performed using Python SciPy.<sup>30</sup>

## 198 2.7 Signal Confinement

### 199 2.7.1 Spatial Profiles

200 To compare the signal confinement spatial profiles were generated. To produce the widefield axial  
201 profile a  $z$ -stack was collected manually. At the end of an imaging trial the micropipette was

202 removed and a  $z$ -stack was collected by moving the plane of focus through the sample between -40  
203 to 40  $\mu\text{m}$  in steps of 1  $\mu\text{m}$  using a stepper motor. Light-field axial profiles ( $xz$ ,  $yz$ ) were generated  
204 by synthetically refocusing and deconvolving at different depths of focus from the light-field taken  
205 with the cell in the native imaging plane. Lateral profiles ( $xy$ ) were then generated by taking a line  
206 plot through the cell on widefield or reconstructed light-field images at the plane of best focus. The  
207 spatial signal confinement is reported from the Full-Width at Half-Maximum (FWHM). Friedman's  
208 Two-Way Analysis of Variance by Ranks was performed between the FWHMs from widefield and  
209 light-field volumes reconstructed with synthetic refocusing and 3-iteration RL 3D deconvolution.

210 The spatial profiles from single-cells were generated from either a single static image in the case  
211 of light-field frames or a stack of widefield frames. However, in bulk-labeled slices the background  
212 signal was very large and the spatial profiles were generated from the activation map described in  
213 Section 3. Maximum intensity projections were taken through  $xy$ ,  $xz$ , and  $yz$ .

#### 214 2.7.2 Temporal Spatial Profiles

215 Temporal spatial profiles were produced from single cells to determine the axial spread of the  
216 calcium fluorescence response. Light-field axial profiles were generated as in Section 2.7.1. Time  
217 courses were extracted for each depth from either a somatic or nearby dendritic ROI.  $\Delta F/F$  was  
218 calculated using eq. 5 in Section 2.5.1. A line plot across the axial range was generated from the  
219 sum over time.

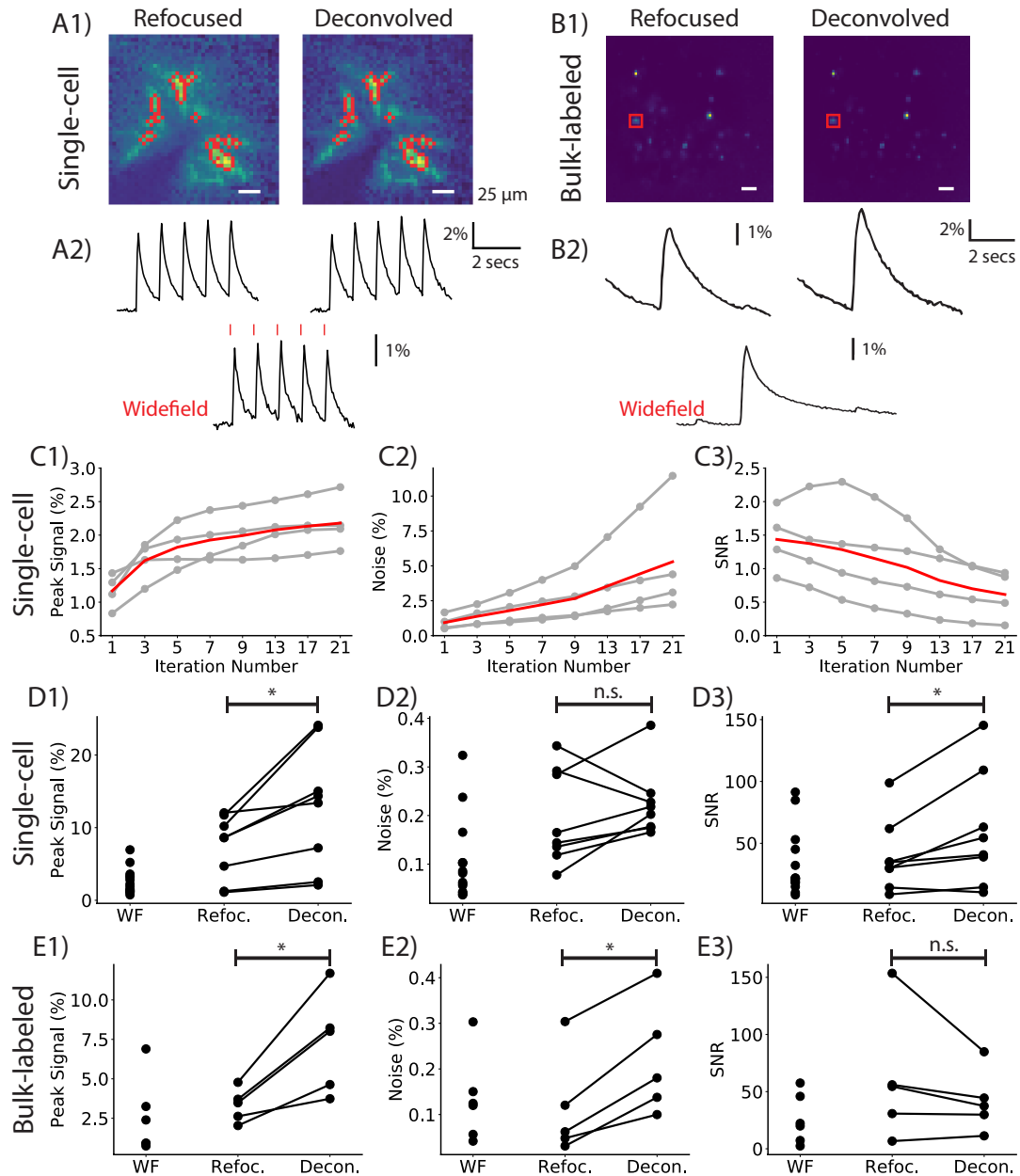


**Fig 2** A comparison of calcium transient tSNR for widefield (WF) and light fields reconstructed with temporal refocusing or RL 3D deconvolution. A1 and B1 show the calcium activation maps of planes reconstructed from light fields containing a single labeled cell (A1) and multiple cells in bulk-labeled slices (B1) using synthetic refocusing and RL 3D deconvolution (3-iteration) algorithms. Calcium transient time series (A2,B2) were extracted from the mean pixel intensities of the ROIs (outlined in red). As deconvolution iteration number increases, so does the peak signal (C1) and noise (C2) respective to time series reconstructed with synthetic refocusing for matching ROIs, ultimately reducing the SNR (C3). The gray traces are from separate single-cell experiments and the red line is the average (n=4 cells). C1-C3 are normalized by the signal, noise, and SNR of signals extracted from the same ROIs in the synthetically refocused planes. D and E compare peak signal (%), noise (%), and SNR between time series extracted from WF images series, refocused and deconvolved (3-iteration RL) light fields.



## 220 **3 Results**

### 221 *3.1 Synthetic refocusing enables fast, high SNR light-field reconstruction*

222 We compared the performance of light-field reconstruction techniques on the tSNR of CaSIR-1  
223 signals extracted from both single-cell (intracellularly loaded) and bulk-labeled slices. We recon-  
224 structed volumetric light-field time series from 4 single cells (Figure 2A & Supplementary videos  
225 S2A & B) and 4 bulk-labeled slices (Figure 2B) with synthetic refocusing and Richardson-Lucy 3D  
226 deconvolution. For single-cell trials, calcium transients were stimulated by applying suprathresh-  
227 old current pulses (red lines) to the soma in whole-cell current clamp (Figure 2A2). Calcium  
228 transients from bulk-labeled slices were captured after a single cell was stimulated within the field  
229 of view (Figure 2A2). We interleaved widefield and light-field acquisitions to facilitate comparison  
230 of functional signals extracted from matched ROIs. Time courses were extracted from a ROI taken  
231 from the top 2 percentile of pixels at the native focal plane. The SNR, peak signal, and baseline  
232 noise were compared between the two light-field reconstruction algorithms and widefield image  
233 series.

234 Iterative 3D deconvolution algorithms including Richardson-Lucy are known to amplify noise<sup>29</sup>  
235 which increases with iteration number. Therefore, we quantified the effect of iteration number on  
236 the peak signal, noise, and SNR from single-cell trials. light-field time series were deconvolved  
237 with between 1 and 21 iterations. The deconvolved time series were normalized to synthetically  
238 refocused time series generated from the same raw light-fields. On average, the peak signal (%)  
239 increases with iteration number with respect to synthetically refocused light-field time series (Fig-  
240 ure 2C1). Between 1 and 7 iterations, the deconvolved peak signal increases after which it plateaus  
241 with a peak signal around  $2\times$  greater than that achieved by synthetic refocusing. In all trials, as

242 iteration number increases, the noise (%) increases compared to synthetically refocused light-field  
243 time series (Figure 2C2). The deconvolved time series noise was on average the same as synthet-  
244 ically refocused light-field time series after 1 iteration increasing to  $5\times$  greater with 21 iterations.  
245 Therefore, on average, as iteration number increases the SNR reduces (Figure 2C3). The SNR  
246 from deconvolved light-field time series after 1 iteration is on average  $1.5\times$  larger than that of syn-  
247 thetically refocused light-field time series. The SNR from deconvolved and synthetically refocused  
248 trials is the same around 9 iterations. Deconvolution tSNR decreases to half that of synthetically  
249 refocused after 21 iterations.

250 Next, we compared the performance of light-field reconstruction techniques on the SNR from  
251 all trials for both single-cell and bulk-labeled slices. Three-iteration RL deconvolution was chosen  
252 to give the best lateral signal confinement at the highest possible SNR, as detailed in the next  
253 section.

254 The peak signal from single-cell trials (8 trials, 4 cells, 3 mice) was significantly larger when  
255 extracted from light-field time series reconstructed with three-iteration Richardson-Lucy 3D de-  
256 convolution (13.9 [2.4, 23.9]%) compared to synthetic refocusing (8.6 [1.2, 11.8]%; Wilcoxon  
257 matched pairs signed rank,  $n = 8$ ,  $w = 36.0$ ,  $p = 0.01$ ) and single-plane widefield time series (3.2  
258 [1.7, 5.6]%; Figure 2D1). The baseline noise did not differ between light-field time series re-  
259 constructed with three-iteration 3D deconvolution (0.21 [0.17, 0.29]%), those reconstructed with  
260 synthetic refocusing (0.15 [0.11, 0.31]%; Wilcoxon matched pairs signed rank,  $n = 8$ ,  $w = 28.0$ ,  $p$   
261  $= 0.02$ ), and those from widefield time series (0.10 [0.04, 0.26]%; Figure 2D2). The SNR of times  
262 series from three-iteration RL-deconvolved frames (47.6 [13.3, 120.0]) was significantly greater  
263 than that of synthetically refocused frames (32.5 [12.6, 73.0]; Wilcoxon rank sum,  $n = 8$ ,  $w = 25.0$ ,  
264  $p = 0.03$ ) and single-plane widefield time series (21.9 [16.8, 86.2]; Figure 2D3).

265 In bulk-labeled slices (5 trials, 4 cells, 2 mice), the peak signal was significantly greater for  
266 light-field time series reconstructed with three-iteration RL 3D deconvolution (8.0 [4.1, 10.3]%)  
267 compared to synthetically refocused (3.5 [2.3, 4.4]%; Wilcoxon rank sum,  $n = 5$ ,  $w = 15$ ,  $p =$   
268 0.04) and widefield time series (1.7 [0.8, 5.1]%; Figure 2E1). The baseline noise was significantly  
269 larger in three-iteration deconvolved bulk-labeled slices (0.18 [0.12, 0.35]%) compared to synthetic  
270 refocusing (0.06 [0.04, 0.23]%; Wilcoxon rank sum,  $n = 5$ ,  $w = 15$ ,  $p = 0.04$ ), and widefield time  
271 series (0.12 [0.05, 0.22]%; Figure 2E2). The SNR from light-field time series reconstructed with  
272 synthetic refocusing (54.5 [16.3, 114.5]) did not differ from deconvolution-reconstructed trials  
273 (37.4 [18.7, 68.7]; Wilcoxon rank sum,  $n = 5$ ,  $z = 2.0$ ,  $p = 0.14$ ) or widefield trials (21.1 [4.9,  
274 51.7]), Figure 2E3).

275 To enhance edges and reduce noise in bulk-labeled volumes, we modified the objective function  
276 of RL to include a TV regularization term (Figure S1A). Inclusion of the TV term in the RL  
277 deconvolution reduced the total variation of the deconvolved stacks from 0.16 to 0.123 after 10  
278 iterations. However, the mean squared error between TV and non-TV reconstructed volumes was  
279 very small, resulting in identical peak signal, noise, and SNR in the extracted calcium time series  
280 (Figure S1B). Increasing iteration number up to 30 reduced peak signal, and thus SNR, for the  
281 TV-regularized volume (Figure S1C).

### 282 *3.2 Deconvolution reconstruction algorithms provide enhanced spatial signal confinement*

283 We compared the lateral and axial signal confinement of single cells intracellularly labeled with  
284 calcium dye between widefield z-stacks and 3D light-fields reconstructed with synthetic refocus-  
285 ing (Figure 3A2) and RL 3D deconvolution (Figure 3A3 & Supplementary video S2C). To assess  
286 the impact of deconvolution iteration number on spatial confinement, we measured the FWHM of

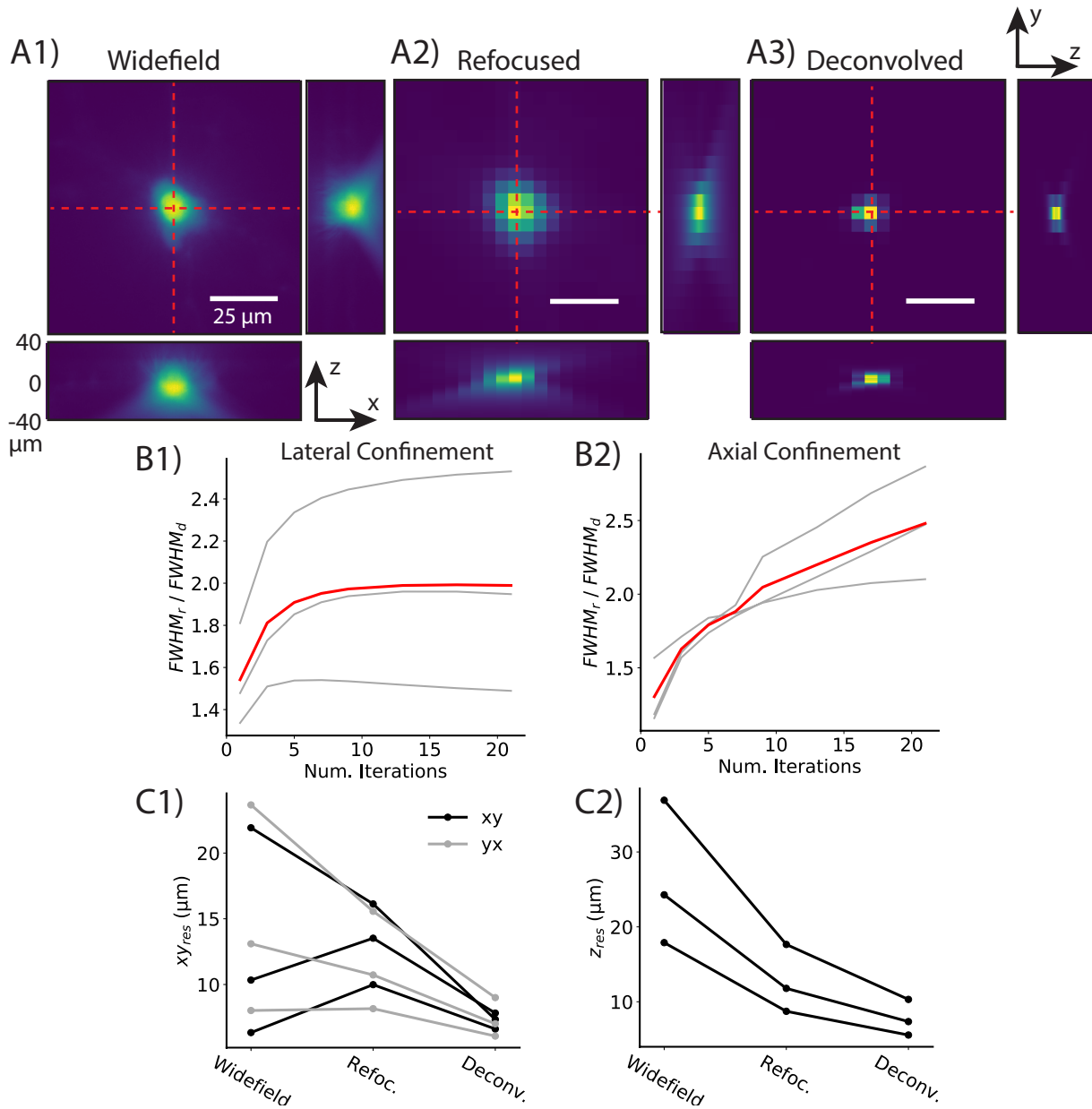


**Fig 3** Deconvolution enhances spatial signal confinement compared to widefield stacks and light-field volumes reconstructed with synthetic refocusing. Lateral and axial profiles from a single-cell filled with CaSiR-1 dye are shown. The lateral profiles are plotted at the native focal plane from widefield stacks (A1), and light-field volumes reconstructed with synthetic refocusing (A2) and 3-iteration Richardson-Lucy deconvolution (A3). The axial profiles have been extracted from the lateral position intersected by the red dashed lines at depths ranging from -40 to +40 μm. Increasing deconvolution iteration number increases both the lateral (B1) and axial (B2) signal confinement compared to synthetically refocused volumes. The deconvolved FWHMs are normalized to that of synthetic refocusing. The gray lines are from three different cells, and the red line is the average. Deconvolved light-fields (3-iteration RL) features better lateral (C1) and axial (C2) spatial confinement than widefield z-stacks and synthetically refocused light-field volumes.

287 lateral and axial profiles, normalized to the FWHM the same profiles in synthetically refocused  
288 volumes. Both the lateral (Figure 3B1) and axial (Figure 3B2) signal confinement increase with  
289 increasing deconvolution iteration number. The red line shows the average for the three cells. The  
290 lateral signal confinement (Figure 3B1) for one iteration is  $1.6\times$  better than synthetically refo-  
291 cused light-field images and plateaus around 7 iterations with a  $2\times$  improvement. The axial signal  
292 confinement (Figure 3B2) for one deconvolution iteration is  $1.4\times$  better than synthetic refocusing  
293 increasing to  $2.5\times$  after 21 deconvolution iterations. Three-iteration Richardson-Lucy deconvolu-  
294 tion was chosen for further analysis as it maximized lateral confinement while maintaining a high  
295 tSNR.

296 The 2D spatial profiles (Figure 3A1-3) clearly show that the light-field images reconstructed  
297 with 3D deconvolution have better spatial signal confinement, both laterally and axially compared  
298 to both those reconstructed with synthetic refocusing and widefield stacks. The spatial profile for  
299 refocused volumes looks similar to widefield, which is expected due to the nature of the reconstruc-  
300 tion. A line plot was taken through the lateral and axial profiles, and the FWHM was calculated  
301 for each of the imaging configurations from 3 cells (Figure 3C1&2). The results are summarized  
302 in Table 1.

303 The lateral signal confinement ( $xy$  &  $yx$ ; Figure 3C1) from light-field images reconstructed  
304 with 3D deconvolution (3-iteration RL) was not significantly better than that of synthetically refo-  
305 cused or widefield stacks (Friedman's Two-Way Analysis of Variance by Ranks;  $xy$ :  $n=3$ ,  $w=2.67$ ,  
306  $p = 0.26$   $yx$ :  $n=3$ ,  $w=4.67$ ,  $p = 0.10$ ). However, 3D deconvolution significantly improved axial sig-  
307 nal confinement ( $xz$ ; Figure 3C2) compared to that of synthetically refocused or widefield stacks  
308 (Friedman's Two-Way Analysis of Variance by Ranks;  $n=3$ ,  $w=6$ ,  $p < 0.05$ ).

309 For the bulk-labeled slices, the low contrast of the raw images precluded segmentation of in-

**Table 1** Summary of FWHM from single-cell labeled spatial profiles. Reported as median [IQR], n=3. \*3-iteration Richardson-Lucy.

	Widefield	Refocused	Deconvolved*	
$xy$	10.3 [7.1, 19.6]	13.5 [10.7, 15.6]	7.3 [6.8, 7.7]	$\mu\text{m}$
$yx$	13.1 [9.0, 21.6]	10.7 [8.7, 14.6]	7.0 [6.3, 8.6]	$\mu\text{m}$
$xz$	17.9 [19.2, 34.4]	11.8 [9.3, 16.5]	7.4 [5.9, 9.7]	$\mu\text{m}$

310 individual cells. The cellular spatial profiles were therefore generated from an activation map (the  
311 variance over time). Maximum intensity projections through  $xz$  and  $yz$  are shown (Figure 4). The  
312 signal confinement for both synthetically refocused and 3D deconvolved light-field volumes en-  
313 abled resolution of a number of active neurons across different focal planes spanning about  $9\ \mu\text{m}$ ,  
314 which is unachievable with any widefield imaging system. The center of mass of each neuron  
315 ranges from depths of  $-5$  to  $+4\ \mu\text{m}$ . The image contrast is higher for 3D deconvolved than for  
316 refocused volumes.

317 Additionally, maximum intensity projections through  $xz$  and  $yz$  were generated with the TV  
318 term (Figure S1D). The TV term at both 10 and 30 iterations did not change the spatial signal  
319 confinement.

### 320 *3.3 Light-field microscopy resolves calcium signals from neuronal dendrites in 3D*

321 Light-field microscopy enables single-frame 3D imaging; therefore, we investigated its application  
322 to resolving calcium signals from neuronal processes in three spatial dimensions. We reconstructed  
323 4D ( $x,y,z,t$ ) light-field volumes from time series and extracted temporal signals from ROIs manu-  
324 ally defined over the cell soma and two dendrites from the activation map.

325 Depth-time plots were extracted from ROIs taken from light-field time series reconstructed  
326 with synthetic refocusing (Figure 5B) and 3D deconvolution (3-iteration RL; Figure 5C). A depth  
327 map cannot be produced from widefield images focused on a single axial plane (Figure 5A).

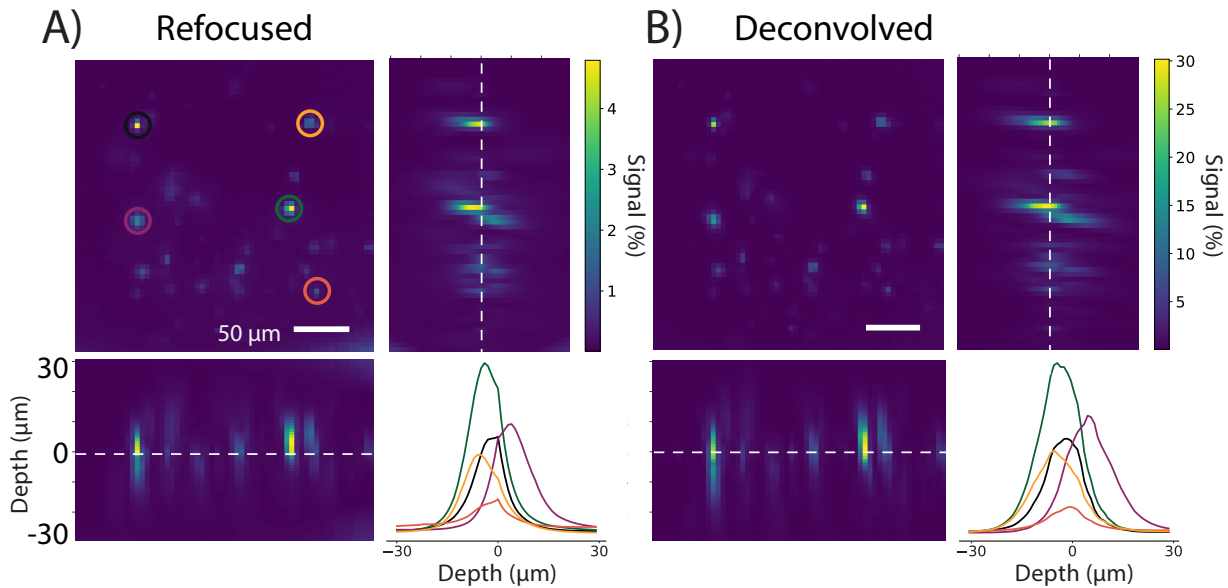


**Fig 4** Reconstructed light-field volumes can distinguish cells from different axial planes in bulk-labeled slices. Planes from bulk-labeled slices were reconstructed from light-field volumes with synthetic refocusing (A) and 3D deconvolution (B, 3-iteration Richardson-Lucy) between -30 and +30 μm in steps of 1 μm. An activation map was generated from the variance over time to identify active neurons. A maximum intensity projection through  $z$  was generated. A  $xz$  and  $yz$  maximum intensity projection shows multiple cells in the field of view spanning different axial planes. The lower right plot in each panel shows the  $z$ -profiles of cellular ROIs circled in the same colors on the image. The center of mass of each neuron ranges in depth from -5 to +4 μm.

328 Somatic calcium transients can be seen across multiple planes in light-field time series recon-  
329 structed with synthetic refocusing (Figure 5B2) and 3D deconvolution (Figure 5C2). The signal as  
330 a function of depth has been summed over time (Figure 5D1). The somatic peak signal is greater  
331 in deconvolved volumetric light-field time series compared to those synthetically refocused, in  
332 agreement with the results from Section 3.

333 The increase in peak signal seen at the extremes of the axial range in the deconvolved light-field  
334 volumes is an artifact of the deconvolution algorithm and how the signal is calculated (eq. 5). The  
335 low baseline fluorescence and small dark signal is overpowered by the large out-of-focus dendritic  
336 fluorescent signal.

337 The peak signal seen in both of the dendrites is greater in deconvolved volumetric light-field  
338 time series (Figure 5C3,4) compared to those synthetically refocused (Figure 5B3,4), in agreement

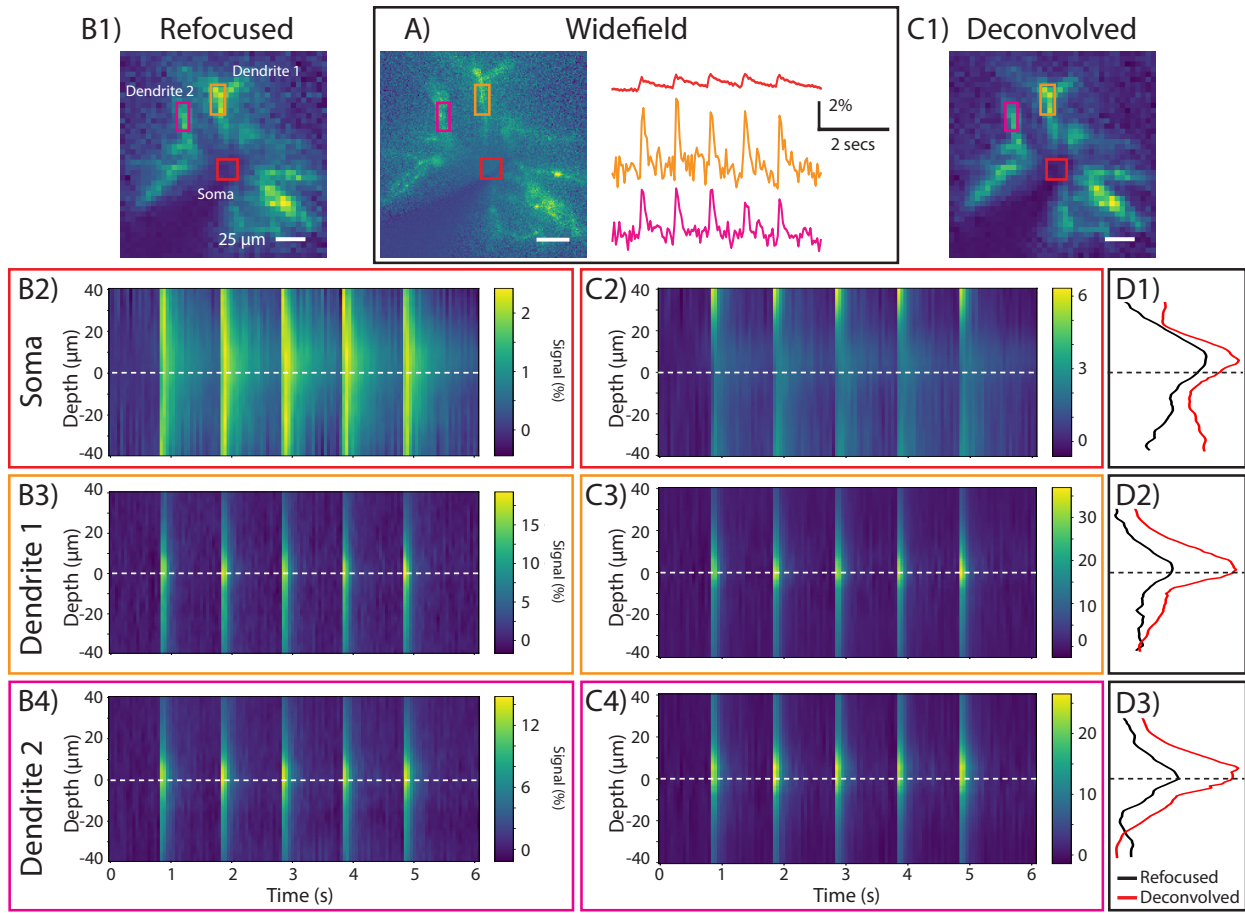


**Fig 5** Calcium signals in dendrites can be observed across axially distinct planes from single-cell light-field volumes. A) shows the activation (or variance) map from a widefield image series with time courses extracted from a somatic ROI (red) and two nearby dendrites (orange, pink). Depth-time plots are shown from the same ROIs reconstructed from a light-field time series with synthetic refocusing (B) and 3D deconvolution (C). D1-3 show the sum of the signal over time as a function of depth in the somatic and dendritic ROIs.

339 with the results from Section 3. From the depth plots it appears that the center of mass from both  
 340 of the dendrite ROIs lie close to the native focal plane ( $\sim 5 \mu\text{m}$ ) whereas the soma signal peaks at  
 341 about 10 microns superficial to the native focal plane (Figure 5D2,3). This indicates that calcium  
 342 transients can be resolved from neuronal subcompartments in axially distinct planes. Furthermore,  
 343 the somatic signals spans a larger depths than the dendritic signals, corresponding the difference  
 344 in their sizes.

345 The decay time, measured by the FWHM of somatic calcium transients at the native focal



346 plane is the same between widefield (0.23 [0.20, 0.27]s, n=3 cells) and light-field time series  
347 reconstructed with synthetic refocusing (soma: 0.24 [0.21, 0.32]s, n=3 cells) and 3D deconvolution  
348 (soma: 0.22 [0.20, 0.40]s, n=3 cells). Moreover, there is no significant difference between the  
349 decay time of somatic and dendritic signals of synthetically refocused (dendrite: 0.139 [0.136,  
350 0.141]s, n=3 cells) or deconvolved (dendrite: 0.132 [0.126, 0.167]s, n=3 cells) light-field time  
351 series.

## 352 **4 Discussion**

353 We resolved CaSiR-1 fluorescence transients in single cells and bulk-labeled live mouse brain  
354 slices. We found that calcium transient tSNR from bulk-labeled slices did not differ between  
355 widefield and light-field time series reconstructed with synthetic refocusing and three-iteration  
356 Richardson-Lucy 3D deconvolution. For single-labeled cells the tSNR was significantly larger for  
357 light-field time series reconstructed with three-iteration Richardson-Lucy 3D deconvolution com-  
358 pared to synthetic refocusing. Increasing the number of deconvolution iterations increased signal  
359 size and noise but reduced tSNR. Increased iteration number also increased axial confinement.  
360 Both light-field reconstruction algorithms, synthetic refocusing and Richardson-Lucy deconvolu-  
361 tion, enabled 3D localization of calcium transients in single dye-loaded neurons and bulk-labeled  
362 slices. Extracting calcium transients from light fields, compared to widefield image time series,  
363 did not incur any penalty in terms of tSNR, while enabling volumetric imaging.

364 The reduction in SNR seen from deconvolved volumes arises from noise amplification due to  
365 lack of regularization.<sup>29</sup> To reduce noise amplification, fewer iteration numbers provide a regu-  
366 larizing effect on the deconvolution.<sup>13</sup> For higher iteration numbers, we attempted to overcome  
367 noise amplification by implementing TV-regularization in the RL deconvolution.<sup>29</sup> However, this

368 yielded no benefit in terms of signal, noise, or SNR in the extracted calcium time series.

369 Richardson-Lucy deconvolution at high iteration numbers decreases tSNR, and moreover in-  
370 creases computational cost compared to synthetic refocusing. In our implementation and hardware,  
371 reconstructing a volume ( $20\ \mu\text{m}$ ) with synthetic refocusing took 40 seconds per frame while RL  
372 deconvolution took 20 seconds per iteration per frame (Processor i7 CPU @ 3.6 GHz, RAM 32  
373 GB). A typical time series consisted of 200 frames ( $2048\times 2048$  pixels, 20 Hz for 10 seconds).  
374 Reconstructing volumes ( $20\ \mu\text{m}$ ) for the full time series took approximately 2 hours with synthetic  
375 refocusing, 3.5 hours 3-iteration RL deconvolution, and 22 hours with 20-iteration RL decon-  
376 volution. Methods to increase speed without the need to use high performance computing are  
377 desirable. Reconstruction speed has been improved by a number of groups through deep learning  
378 solutions.<sup>19,31</sup> However, the improved lateral and axial signal confinement achieved by iterative  
379 deconvolution methods may still motivate its use. We have shown that 3D deconvolution achieves  
380 higher spatial signal confinement than synthetic refocusing with axial confinement increasing at  
381 high iteration numbers. Therefore, to maximize spatial signal confinement a time-consuming iter-  
382 ative deconvolution technique could be beneficial.

383 Deconvolution algorithms leverage the fine sampling of individual projections through the vol-  
384 ume, whereas refocusing cannot. Here we used a coarse deconvolution approach. Lateral oversam-  
385 pling can further improve the lateral signal confinement, providing lateral sampling rates greater  
386 than the native LFM resolution. However, oversampling increases computational cost and was  
387 unnecessary here as the LFM was designed for cellular resolution. We used the original light-  
388 field microscope design.<sup>7</sup> Fourier light-field microscopy, where the microlens array is placed at  
389 the aperture stop of the microscope objective instead of the image plane, has also been shown to  
390 improve the lateral sampling rate even in the degenerate native focal plane.<sup>32-34</sup>

391 Both synthetic refocusing and 3D deconvolution reconstruction algorithms rely on ballistic  
392 photons, limiting their application in highly scattering mammalian brains. To minimize scattering,  
393 we used a red-emitting calcium dye, CaSiR-1 whose emission is less scattered than shorter wave-  
394 length emitting fluorophores. Furthermore, deep near-infrared indicators can be combined with  
395 blue-light sensitive opsins to achieve spectrally cross-talk free all-optical neurophysiology<sup>35,36</sup> or  
396 combined with shorter wavelength emitting fluorophores for imaging in multiple spectral chan-  
397 nels.<sup>37</sup> Nonetheless, scattering limited calcium signal extraction from reconstructed volumes to  
398 depths of approximately 50 microns, within the photon mean free path. Methods to improve signal  
399 extraction in scattering tissue have been demonstrated by computationally extracting fluorescence  
400 sources without reconstruction,<sup>15,20,22,38–40</sup> although reconstruction-less signal extraction cannot  
401 resolve the propagation of calcium signals throughout spatially extended structures such as den-  
402 drites. Combining the principles of confocal microscopy with LFM,<sup>41</sup> selective-volume illumi-  
403 nation,<sup>19,42,43</sup> and/or spatially sparse labelling with genetically-encoded indicators can increase  
404 contrast to enable calcium signal extraction from reconstructed volumes at greater depths.

405 We detected dendritic calcium signals, evoked by back-propagating action potentials, in intra-  
406 cellularly dye loaded single cells. Limited dye diffusion precluded activity detection in distant  
407 processes. Applying LFM to neuronal tissues expressing genetically encoded calcium indica-  
408 tors (GECI) sparsely and strongly may enable tracing of functional signals through dendrites in  
409 three-dimensions, or synaptic mapping. Similar analyses have been performed for sparsely labeled  
410 genetically encoded voltage indicators (GEVIs) with a much lower baseline fluorescence,  $\Delta F/F$ ,  
411 and tSNR than that of the CaSiR-1 calcium dye.<sup>44,45</sup> Quicke *et al.* (2020) also demonstrated ax-  
412 ial resolution of GEVI signals from dendrites at different depths. In combination with the present  
413 study, these results describe the LFM's capacity to resolve function neuronal signals volumetrically

414 at subcellular resolution in both low and high SNR regimes.

415 LFM captures 3D information with significantly reduced imaging time and bleaching com-  
416 pared to widefield. Generating similar 3D volumes in widefield would require physical refocusing  
417 of the objective in between trials. Our comparison of widefield trials to light-field trials recon-  
418 structed at the same axial plane revealed no penalty in terms of extracted calcium transient tSNR  
419 for light fields, which additionally enabled extraction of “in-focus” calcium transients from axially  
420 separated planes. Optically, implementing LFM is simple and low-cost, requiring only the intro-  
421 duction an off-the-shelf MLA at the native imaging plane of a standard widefield epifluorescence  
422 microscope. Cost-effective sCMOS cameras feature sensitivities and bandwidths well adapted to  
423 calcium LFM. Calcium imaging applications requiring high volume acquisition rates can readily  
424 benefit from LFM’s ability to trade spatial resolution for the ability to excite and image fluores-  
425 cence simultaneously throughout a volume.

426 These results demonstrate the capabilities and limitations of two light-field reconstruction al-  
427 gorithms for high SNR calcium fluorescence imaging. The trade-offs described above highlight  
428 the importance of adapting the volume reconstruction strategy to the scientific goals and require-  
429 ments of future neurophysiology experiments. For example, applications requiring online analysis  
430 to guide the experimental protocols would benefit from the speed and simplicity of synthetic re-  
431 focusing or low iteration-number 3D RL deconvolution. We found that calcium signal extraction  
432 from volumes reconstructed with 3-iteration 3D RL deconvolution yielded high tSNR while bring-  
433 ing lateral signal confinement near to the maximum. However, higher iteration numbers, while  
434 decreasing tSNR, continued improving the axial confinement. These results demonstrate the im-  
435 portance characterizing and balancing tSNR, spatial signal confinement, and computational cost  
436 when selecting a volume reconstruction method for functional LFM applications.

437 *Disclosures*

438 The authors declare no conflicts of interest.

439 *Acknowledgments*

440 The authors would like to thank Yu Liu, Simon Schultz, and Ann Go for their technical as-  
441 sistance. The authors would also like to thank the Imperial College Research Computing Ser-  
442 vice. This project was funded by the Biotechnology and Biological Sciences Research Council  
443 (BB/R009007/1). National Institutes of Health (U01NS090501, U01NS099573, U01MH109091);  
444 Wellcome Trust Seed Award (201964/Z/16/Z); and a Royal Academy of Engineering Research  
445 Fellowship (RF1415/14/26).

446 **Author Contributions**

447 CLH, PQ, and AJF conceived and designed the experiments. CLH and AJF designed the light-  
448 field optics. CLH performed experiments. CLH, PQ, and AJF designed the analysis. PQ, PS, HVJ,  
449 and PLD developed the deconvolution approach. CLH analyzed the data and wrote the paper. All  
450 authors contributed to manuscript revision and approved the final manuscript.

451 **Data, Materials, and Code Availability**

452 The datasets and code generated for this study are available on request to the corresponding author.

453 *References*

- 454 1 F. Ali and A. C. Kwan, "Interpreting in vivo calcium signals from neuronal cell bodies, axons,  
455 and dendrites: a review," *Neurophotonics* **7**(1), 011402 (2019).

- 456 2 H. Dana, B. Mohar, Y. Sun, *et al.*, “Sensitive red protein calcium indicators for imaging  
457 neural activity,” *Elife* **5**, e12727 (2016).
- 458 3 M. Z. Lin and M. J. Schnitzer, “Genetically encoded indicators of neuronal activity,” *Nature*  
459 *neuroscience* **19**(9), 1142 (2016).
- 460 4 J. Platisa and V. A. Pieribone, “Genetically encoded fluorescent voltage indicators: are we  
461 there yet?,” *Current opinion in neurobiology* **50**, 146–153 (2018).
- 462 5 V. Grenier, B. R. Daws, P. Liu, *et al.*, “Spying on neuronal membrane potential with ge-  
463 netically targetable voltage indicators,” *Journal of the American Chemical Society* **141**(3),  
464 1349–1358 (2019).
- 465 6 M. A. Popovic, N. Carnevale, B. Rozsa, *et al.*, “Electrical behaviour of dendritic spines as  
466 revealed by voltage imaging,” *Nature Communications* **6** (2015).
- 467 7 M. Levoy, R. Ng, A. Adams, *et al.*, “Light field microscopy,” *ACM SIGGRAPH 2006 Papers*  
468 *on - SIGGRAPH '06* , 924 (2006).
- 469 8 M. Broxton, L. Grosenick, S. Yang, *et al.*, “Wave optics theory and 3-D deconvolution for  
470 the light field microscope,” *Optics Express* **21**(21), 25418 (2013).
- 471 9 P. Quicke, C. L. Howe, P. Song, *et al.*, “Calculation of high numerical aperture lightfield  
472 microscope point spread functions,” in *Computational Optical Sensing and Imaging, CW4A-*  
473 *2*, Optical Society of America (2019).
- 474 10 W. H. Richardson, “Bayesian-Based Iterative Method of Image Restoration\*,” *Journal of the*  
475 *Optical Society of America* **62**, 55 (1972).
- 476 11 L. B. Lucy, “An iterative technique for the rectification of observed distributions,” *The Astro-*  
477 *nomical Journal* **79**, 745 (1974).

- 478 12 M. E. Daube-Witherspoon and G. Muehllehner, “An Iterative Image Space Reconstruction  
479 Algorithm Suitable for Volume ECT,” *IEEE Transactions on Medical Imaging* **5**, 61–66  
480 (1986).
- 481 13 M. Bertero, P. Boccacci, and V. Ruggiero, *Inverse Imaging with Poisson Data*, IOP Publish-  
482 ing, Bristol (2018).
- 483 14 R. Prevedel, Y. G. Yoon, M. Hoffmann, *et al.*, “Simultaneous whole-animal 3D imaging of  
484 neuronal activity using light-field microscopy,” *Nature Methods* **11**(7), 727–730 (2014).
- 485 15 N. C. Pégard, H.-Y. Liu, N. Antipa, *et al.*, “Compressive light-field microscopy for 3D neural  
486 activity recording,” *Optica* **3**(5), 517 (2016).
- 487 16 L. Cong, Z. Wang, Y. Chai, *et al.*, “Rapid whole brain imaging of neural activity in freely  
488 behaving larval zebrafish (*Danio rerio*),” *eLife* **6** (2017).
- 489 17 M. A. Taylor, T. Nöbauer, A. Pernia-Andrade, *et al.*, “Brain-wide 3d light-field imaging of  
490 neuronal activity with speckle-enhanced resolution,” *Optica* **5**(4), 345–353 (2018).
- 491 18 S. Aimon, T. Katsuki, T. Jia, *et al.*, “Fast near-whole-brain imaging in adult drosophila during  
492 responses to stimuli and behavior,” *PLoS biology* **17**(2), e2006732 (2019).
- 493 19 Z. Wang, L. Zhu, H. Zhang, *et al.*, “Real-time volumetric reconstruction of biological dynam-  
494 ics with light-field microscopy and deep learning,” *Nature Methods* **18**(5), 551–556 (2021).
- 495 20 T. Nöbauer, O. Skocek, A. J. Pernía-Andrade, *et al.*, “Video rate volumetric Ca<sup>2+</sup> imaging  
496 across cortex using seeded iterative demixing (SID) microscopy,” *Nature Methods* **14**(8),  
497 811–818 (2017).
- 498 21 L. Grosenick, M. Broxton, C. K. Kim, *et al.*, “Identification of cellular-activity dynamics  
499 across large tissue volumes in the mammalian brain,” *bioRxiv* , 132688 (2017).

- 500 22 O. Skocek, T. Nöbauer, L. Weilguny, *et al.*, “High-speed volumetric imaging of neuronal  
501 activity in freely moving rodents,” *Nature Methods* **15**(June), 1–4 (2018).
- 502 23 T. Egawa, K. Hanaoka, Y. Koide, *et al.*, “Development of a far-red to near-infrared fluores-  
503 cence probe for calcium ion and its application to multicolor neuronal imaging,” *Journal of*  
504 *the American Chemical Society* **133**(36), 14157–14159 (2011).
- 505 24 C. L. Howe, P. Quicke, P. Song, *et al.*, “Comparing wide field to 3d light field for imaging red  
506 calcium transients in mammalian brain,” in *Optics and the Brain*, BTu2C–4, Optical Society  
507 of America (2020).
- 508 25 J. T. Ting, B. Kalmbach, P. Chong, *et al.*, “A robust ex vivo experimental platform for  
509 molecular-genetic dissection of adult human neocortical cell types and circuits,” *Scientific*  
510 *reports* **8**(1), 1–13 (2018).
- 511 26 R. Franconville, G. Revet, G. Astorga, *et al.*, “Somatic calcium level reports integrated  
512 spiking activity of cerebellar interneurons in vitro and in vivo,” *Journal of neurophysiology*  
513 **106**(4), 1793–1805 (2011).
- 514 27 A. D. Edelstein, M. A. Tsuchida, N. Amodaj, *et al.*, “Advanced methods of microscope  
515 control using  $\mu$ Manager software.,” *Journal of biological methods* **1**(2), 10 (2014).
- 516 28 R. Ng, M. Levoy, M. Brédif, *et al.*, “Light Field Photography with a Hand-Held Plenoptic  
517 Camera – Stanford Tech Report CTSR 2005-02,” tech. rep. (2005).
- 518 29 N. Dey, L. Blanc-feraud, C. Zimmer, *et al.*, “Richardson-Lucy Algorithm with Total Vari-  
519 ation Regularization for 3D Confocal Microscope Deconvolution,” *Microscopy Research &*  
520 *Technique* **69**(4), 260–266 (2006).



- 521 30 P. Virtanen, R. Gommers, T. E. Oliphant, *et al.*, “SciPy 1.0: Fundamental Algorithms for  
522 Scientific Computing in Python,” *Nature Methods* **17**, 261–272 (2020).
- 523 31 J. Page, F. Saltarin, Y. Belyaev, *et al.*, “Learning to reconstruct confocal microscopy stacks  
524 from single light field images,” *arXiv preprint arXiv:2003.11004* (2020).
- 525 32 C. Guo, W. Liu, X. Hua, *et al.*, “Fourier light-field microscopy,” *Opt. Express* **27**, 25573–  
526 25594 (2019).
- 527 33 A. Stefanoiu, G. Scrofani, G. Saavedra, *et al.*, “What about computational super-resolution in  
528 fluorescence fourier light field microscopy?,” *Optics Express* **28**(11), 16554–16568 (2020).
- 529 34 F. L. Liu, G. Kuo, N. Antipa, *et al.*, “Fourier diffuserscope: single-shot 3d fourier light field  
530 microscopy with a diffuser,” *arXiv preprint arXiv:2006.16343* (2020).
- 531 35 J. Akerboom, N. Carreras Calderón, L. Tian, *et al.*, “Genetically encoded calcium indica-  
532 tors for multi-color neural activity imaging and combination with optogenetics,” *Frontiers in*  
533 *molecular neuroscience* **6**, 2 (2013).
- 534 36 N. S. Soor, P. Quicke, C. L. Howe, *et al.*, “All-optical crosstalk-free manipulation and read-  
535 out of chronos-expressing neurons,” *Journal of physics D: Applied physics* **52**(10), 104002  
536 (2019).
- 537 37 M. Oheim, M. van’t Hoff, A. Feltz, *et al.*, “New red-fluorescent calcium indicators for op-  
538 togenetics, photoactivation and multi-color imaging,” *Biochimica et Biophysica Acta (BBA)-*  
539 *Molecular Cell Research* **1843**(10), 2284–2306 (2014).
- 540 38 P. Song, H. V. Jadan, C. L. Howe, *et al.*, “3d localization for light-field microscopy via con-  
541 volutional sparse coding on epipolar images,” *IEEE Transactions on Computational Imaging*  
542 **6**, 1017–1032 (2020).

- 543 39 P. Song, H. V. Jadan, C. L. Howe, *et al.*, “Model-inspired deep learning for light-field mi-  
544 croscopy with application to neuron localization,” in *ICASSP 2021-2021 IEEE International*  
545 *Conference on Acoustics, Speech and Signal Processing (ICASSP)*, 8087–8091, IEEE (2021).
- 546 40 H. Verinaz-Jadan, P. Song, C. L. Howe, *et al.*, “Deep learning for light field microscopy using  
547 physics-based models,” in *2021 IEEE 18th International Symposium on Biomedical Imaging*  
548 *(ISBI)*, 1091–1094, IEEE (2021).
- 549 41 Z. Zhang, L. Bai, L. Cong, *et al.*, “Imaging volumetric dynamics at high speed in mouse and  
550 zebrafish brain with confocal light field microscopy,” *Nature Biotechnology* , 1–10 (2020).
- 551 42 T. V. Truong, D. B. Holland, S. Madaan, *et al.*, “High-contrast, synchronous volumetric  
552 imaging with selective volume illumination microscopy,” *Communications biology* **3**(1), 1–8  
553 (2020).
- 554 43 S. Madaan, K. Keomanee-Dizon, M. Jones, *et al.*, “Single-objective selective-volume illumi-  
555 nation microscopy enables high-contrast light-field imaging,” *Optics Letters* **46**(12), 2860–  
556 2863 (2021).
- 557 44 P. Quicke, C. L. Howe, P. Song, *et al.*, “Subcellular resolution three-dimensional light-field  
558 imaging with genetically encoded voltage indicators,” *Neurophotonics* **7**(3), 1 – 19 (2020).
- 559 45 P. Quicke, C. Song, E. J. McKimm, *et al.*, “Single-neuron level one-photon voltage imaging  
560 with sparsely targeted genetically encoded voltage indicators,” *Frontiers in cellular neuro-*  
561 *science* **13**, 39 (2019).

562 **Carmel L. Howe** is a research associate at Imperial College London, UK. She received her MEng  
563 and Ph.D. degrees in Electrical and Electronic Engineering from the University of Nottingham in

564 2014 and 2018, respectively. She is currently developing a new high-speed, high-throughput, three-  
565 dimensional imaging modality based on light-field microscopy to track network-level neuronal  
566 activity in the mammalian brain. Her research combines the fields of neurophysiology, optical  
567 engineering, signal and image processing.

568 **Peter Quicke** is postdoctoral research associate in the Department of Bioengineering at Imperial  
569 College London. He received his MSci. (with BSc.) degree in Physics in 2014, an MRes. in Neu-  
570 rotechnology in 2015 and his Ph.D. in 2019. His current research interests include computational  
571 microscopy and functional voltage imaging.

572 **Pingfan Song** is a research associate at Imperial College London. He obtained the Ph.D. degree  
573 at University College London (UCL), the master and bachelor degree both at Harbin Institute of  
574 Technology (HIT). His research interests lie in signal/image processing, machine learning and  
575 computational imaging with applications on a variety of image modalities.

576 **Pier Luigi Dragotti** received the Laurea degree (summa cum laude) in electronic engineering  
577 from University Federico II, Naples, Italy, in 1997, the master's degree in communications sys-  
578 tems from the Swiss Federal Institute of Technology of Lausanne (EPFL), Switzerland, in 1998,  
579 and the Ph.D. degree from EPFL, Switzerland, in April 2002. He has held several visiting posi-  
580 tions. In particular, he was a visiting student at Stanford University, Stanford, CA, USA, in 1996, a  
581 Summer Researcher at the Mathematics of Communications Department, Bell Labs, Lucent Tech-  
582 nologies, Murray Hill, NJ, USA, in 2000, and a Visiting Scientist at the Massachusetts Institute of  
583 Technology (MIT) in 2011. He is currently a Professor of signal processing with the Electrical and  
584 Electronic Engineering Department, Imperial College London. Before joining Imperial College in

585 November 2002, he was a Senior Researcher at EPFL, working on distributed signal processing  
586 for sensor networks for the Swiss National Competence Center in Research on Mobile Informa-  
587 tion and Communication Systems. His research interests include sampling theory, wavelet theory  
588 and its applications, sparsity-driven signal processing with application in image super-resolution,  
589 neuroscience, and computational imaging. He was the Technical Co-Chair of the European Signal  
590 Processing Conference in 2012, an Associate Editor of the IEEE Transactions on Image Processing  
591 from 2006 to 2009, a member of the IEEE Image, Video and Multidimensional Signal Processing  
592 Technical Committee, and a member of the IEEE Signal Processing Theory and Methods Technical  
593 Committee. He was also a recipient of the ERC Investigator Award. He is currently the Editor-in-  
594 Chief of the IEEE Transactions on Signal Processing, and a member of the IEEE Computational  
595 Imaging Technical Committee and a Fellow of the IEEE.

596 **Amanda J. Foust** is a Royal Academy of Engineering Research Fellow and Lecturer in the De-  
597 partment of Bioengineering at Imperial College London. She studied Neuroscience with emphasis  
598 in computation and electrical engineering (BSc) at Washington State University, and Neuroscience  
599 (MPhil, PhD) at Yale University. The aim of her research programme is to engineer bridges be-  
600 tween cutting-edge optical technologies and neuroscientists to acquire new, ground-breaking data  
601 on how brain circuits wire, process, and store information.

602 Biographies and photographs of the other authors are not available.